An Updated View of Solar Eruptive Flares and the Development of Shocks and CMEs: History of the 2006 December 13 GLE-Productive Extreme Event*

Victor V. Grechnev, Valentin I. Kiselev, Arkadiy M. Uralov, Nataliya S. Meshalkina, and Alexey A. Kochanov

Institute of Solar-Terrestrial Physics SB RAS, Lermontov St. 126A, Irkutsk 664033, Russia

grechnev@iszf.irk.ru

Abstract

An extreme 2006 December 13 event marked the onset of the Hinode era, being the last major flare in the solar cycle 23 observed with NoRH and NoRP. The event produced a fast CME, strong shock, and a big particle event responsible for GLE70. We endeavor to clarify the relations between the eruptions, shock wave, and flare, and to shed light on a debate over the origin of energetic protons. One concept relates it to flare processes. Another one associates the acceleration of ions with a bow shock driven by a CME at (2–4) $R_\odot$. The latter scenario is favored by a delayed particle release time after the flare. However, our previous studies have established that a shock wave is typically excited by an impulsively erupting magnetic rope (future CME core) during the flare rise, while the outer CME surface evolves from an arcade whose expansion is driven from inside. Observations of the 2006 December 13 event reveal two shocks following each other, whose excitation scenario contradicts the delayed CME-driven bow-shock hypothesis. Actually, the shocks developed much earlier, and could accelerate protons still before the flare peak. Then, the two shocks merged into a single stronger one, and only decelerated and dampened long afterwards.

Key words: shock waves — Sun: coronal mass ejections (CMEs) — Sun: flares — Sun: particle emission — Sun: radio radiation

1. Introduction

Eruptions of solar magnetized plasmas and accompanying phenomena present most vigorous manifestations of the solar activity. General relations between eruptions and flares were theoretically understood in the 1960–1970s, and constituted the basis of the standard flare model (called as CSHKP: Carmichael 1964; Sturrock 1966; Hirayama 1974; Kopp & Pneuman 1976). Associations of eruptive flares with coronal shock waves were predicted by Uchida (1968) and Hirayama (1974). Later studies (e.g., Chen 1989; Antiochos et al. 1999; Moore et al. 2001; Uralov et al. 2002; and others) supplemented the model with ideas about the initiation of coronal mass ejections (CMEs).

Despite the rather long history of theoretical concepts of solar eruptive flares, difficulties still remain in establishing connections between the eruptions, flares, CMEs, and shock waves in particular events. There is no consensus concerning such questions as the excitation scenario of shock waves. Recent observations promise noticeable updates of model concepts. On the other hand, progress in understanding the listed phenomena is currently urged by requirements of modern industry, power, transport, and other high-technology systems.

Eruptions and associated phenomena can produce severe space weather disturbances. CMEs carry clouds of magnetized plasmas that can reach Earth and cause geomagnetic storms. Associated shock waves can also affect space weather. Eruptions are accompanied by flare emissions from radio waves up to gamma rays. Solar eruptive events somehow accelerate electrons and protons to high energies. Intense fluxes of accelerated protons sometimes reach the Earth orbit, while being hazardous for equipment and astronauts in space; further, people on aircraft during high-latitude flights are exposed to secondary particles.

The origin of solar energetic particles is still vague (see, e.g., Kallenrode 2003). There are two major competing concepts concerning the acceleration of high-energy heavy particles in solar events. One concept relates their origin with flare processes within an active region (e.g., Klein & Trottet 2001). Another one relates the acceleration of protons and heavier ions up to high energies with shock waves associated with CMEs (e.g., Cliver et al. 1982; Reames 1999). Specifying temporal properties of the processes, which might be related to the acceleration of protons, is among important issues of both solar physics and space weather forecasting.

In the widely accepted conjectural scenario of particle acceleration by a shock front, the shock wave is supposed to develop as a bow shock driven by the outer surface of a super-Alfvénic CME (e.g., Reames 2009; Aschwanden 2012). One of the arguments in favor of this scenario is an apparent delay of the extrapolated solar particle release time relative to flare emissions. This circumstance is considered "*as further evidence that the particles are accelerated by the shock wave that forms late in the event, when the CME driver of the shock reaches 2 or 3 solar radii*" [heliocentric distance, or the height above the solar surface of (1–2) $R_\odot$, Reames 2009]. The concept of bow shock originates from an analogy with the problem of supersonic plasma flow around the surface of a solid or elastic body

---

* Dedicated to the memory of T. Kosugi.

associated with the magnetic bubble of a CME. Two circumstances are important here: (i) the flow around the body occurs with the existence of a stagnation point of the plasma flow at the surface of the body, and (ii) the motion velocity of this stagnation point exceeds the ambient fast-mode speed. However, at the CME formation stage, the analogy with such a plasma flow does not apply, even though this flow is a subsonic one. At this stage, the CME magnetic bubble extrudes surrounding magnetoplasmas away almost omnidirectionally, thus forming an extensive disturbed zone of compression around it. This zone is comparable in size with the initial CME. The front of this zone is a weak discontinuity running with the ambient fast-mode speed. The fast-mode speed of the moving plasmas within this zone is higher than the pre-event ambient fast-mode speed. The boundary of the CME magnetic bubble, i.e., its outer separatrix surface, is already detectable at this stage due to the growing plasma compression ahead. In the bow-shock concept, the CME size and speed ($V_{\mathrm{CME}} > V_{\mathrm{fast}}$) determine the position and intensity of the stationary shock ahead of the CME. Kinematical differences of the structural CME components preceding the appearance of the shock are not discussed concerning the bow-shock concept. A significant distinction of their accelerations from the self-similar regime is among these differences.

However, the results of Grechnev et al. (2011a, 2011b) do not support the bow-shock excitation scenario in the low corona. Instead, it turns out that shock waves are excited by the impulsive-piston mechanism during the rise phase of a flare. In the impulsive-piston concept, the wave disturbance is essentially non-stationary. Its intensity is determined by the acceleration of the piston. The major role of the acceleration can be demonstrated in the following way. The magnetic flux rope expands in both the major and minor radii simultaneously. Accordingly, the radiation of the magnetosonic wave by an element of the flux rope can be divided into the dipole and monopole components. The intensity of each component is proportional to the squared acceleration, with which each radius changes. The sharpest portion in the velocity profile of the disturbance propagating away from the piston forms approximately at the same time as the acceleration reaches its maximum. This portion is a place, where the discontinuity (i.e., shock) starts to form. As our previous analyses have shown, the wave front, which appears in the disturbed zone surrounding a CME, is excited by a sharp impulsive eruption inside the developing CME, where a steep outward-directed falloff of the Alfvén speed favors amplification of the wave and rapid formation of the discontinuity in $\sim 10^2$ s (Afanasyev et al. 2013). The kinematics of the whole CME determines whether or not the heading portion of the wave transforms into bow shock afterwards.

This scenario is confirmed by Grechnev et al. (2011a), who briefly discussed moderate eruptive flares. It is reasonable to check what occurred in a major event, which has produced a big near-Earth enhancement of high-energy proton flux. The extreme 2006 December 13 solar event, observed in detail with many instruments, provides this opportunity.

Many papers have already addressed various aspects of this event. At least two eruptive episodes have been revealed (e.g., Asai et al. 2008; Sterling et al. 2011). The event produced large-scale disturbances, such as 'EUV waves' and dimmings, the latter being both a deep depressions near the active region and shallower remote dimmings (e.g., Attrill et al. 2010). Liu et al. (2008) followed the related CME and shock wave to the Earth orbit, and then up to 2.7 au. Several studies addressed the flare (e.g., Jing et al. 2008; Ning 2008). Some attempts have already been made to find out the origin of near-Earth protons (e.g., Li et al. 2009; Reames 2009; Firoz et al. 2011, 2012).

Nevertheless, some important questions remain unanswered. We are not aware of kinematic measurements of eruptions. Relations between the eruptions and extreme flare have not been revealed. The origin and onset time of the shock wave still remains hypothetical. Some conclusions do not stand against observations, or contradict each other. For example, it is difficult to reconcile the conclusion of Sterling et al. (2011) that the major eruption occurred away from the strong fields, with the result of Jing et al. (2008) that the high-energy release regions tend to be concentrated in local strong-field regions. There is a contradiction between the conclusions of Li et al. (2009), who argued in favor of flare-acceleration of solar energetic particles, and the conclusions of Firoz et al. (2011, 2012), who favor shock-acceleration of GLE particles.

In the present study we endeavor to shed further light on the listed issues based on the approaches and techniques developed by Grechnev et al. (2011a), and briefly described our findings in section 2. To reach the purposes listed above, we firstly reveal in subsection 3.1 the features of the major phase of the event from its time profiles. In subsection 3.2, we describe measurements of the kinematical characteristics of eruptions based on images observed with the X-Ray Telescope (XRT: Golub et al. 2007) and the Solar Optical Telescope (SOT: Suematsu et al. 2008; Tsuneta et al. 2008) on Hinode (Kosugi et al. 2007). We then co-ordinate the eruptions with the milestones of the extreme flare shown by the microwave total flux light curves recorded with the Nobeyama Radio Polarimeters (NoRP: Torii et al. 1979; Nakajima et al. 1985). Subsection 3.3 considers the development of the extreme flare based on microwave images produced with the Nobeyama Radioheliograph (NoRH: Nakajima et al. 1994), along with NoRP, XRT, and SOT observations starting from the early onset of the flare and up to the end of the second flare peak. In this way, we address the circumstances responsible for the extreme properties of the event. Subsection 3.4 reveals near-surface traces of two shock waves following each other, whose onset times and positions quantitatively indicate their excitation by two major eruptions. Subsection 3.5 confirms this result by an analysis of the type II bursts in the dynamic radio spectrum. Subsection 3.6 discusses the CME, manifestations of the shock in its structure, and their correspondence with the shock waves revealed in previous sections. Section 4 coordinates the results into a consistent picture of the whole event, and addresses some of the contradicting conclusions drawn previously. The outcome of the analysis and its implications are summarized in section 5.

2. Measurement Techniques

Imaging observations provide important visual information about eruptions, wavelike disturbances, and flares. In addition,

quantitative kinematical measurements of moving features can shed light on causal relations between the listed phenomena. Such measurements are complicated by difficulties to follow an expanding feature in question due to its rapidly decreasing brightness or opacity, while concurrent flare emissions are very bright. Difficulties to detect an eruptive feature in all images of interest lead to large uncertainties in its position. A traditional way to measure velocities and accelerations by the differentiation of distance-time measurements causes a large scatter of the results. To overcome this difficulty, we describe the kinematics of eruptions and wavelike disturbances by analytic functions and calculate kinematical plots by means of integration or differentiation of the analytic fit, rather than the measurements. The distance-time measurements are used as a starting estimate of kinematical parameters, and then these parameters are adjusted to outline the measured feature in a best way. Our ultimate criterion is to follow the motion of an analyzed feature in images as closely as possible.

2.1. Motions of Eruptions

Several studies (e.g., Zhang et al. 2001; Maričić et al. 2007; Temmer et al. 2008, 2010; Grechnev et al. 2011a, 2014) have concluded that the acceleration of an eruption or a CME occurs impulsively and temporally close to an associated HXR burst. Using this fact, we considered the initial v_0 and final v_1 velocities of an eruption to be nearly constant, and fit its acceleration with a Gaussian, $a = (v_1 - v_0)\exp\{-[(t-t_0)/\tau_{\rm acc}]^2/2\}/(\sqrt{2\pi}\tau_{\rm acc})$. Here, $\tau_{\rm acc}\sqrt{8\ln 2}$ is the FWHM of the acceleration time profile centered at time t_0. In cases of more complex kinematics, we used a combination of Gaussians and adjusted their parameters manually.

With a rather accurately estimated effective duration and center time of the acceleration, its actual shape is rather uncertain because of double integration in calculating the height-time plot, which is directly compared with the observations. However, the acceleration plot is not expected to contain features shorter than the Alfvén time inside the measured eruption.

2.2. Waves

A simple model (Grechnev et al. 2008b, 2011a, 2011b) describes the propagation of impulsively excited shock waves in plasma with a radial power-law density falloff, δ, from an eruption center, $n = n_0(x/h_0)^{-\delta}$. Here, x is the distance, and n_0 is the density at a distance of $h_0 \approx 100\,{\rm Mm}$ (close to the scale height). The propagation of the global front of such a shock wave is almost insensitive to the magnetic field, but is determined by the plasma density distribution, $x(t) \propto t^{2/(5-\delta)}$. This equation is more convenient to use in the form $x(t) = x_1[(t-t_0)/(t-t_1)]^{2/(5-\delta)}$, where t and x are the current time and distance, t_0 is the wave onset time, and (t_1, x_1) correspond to one of the measured fronts.

For the shock propagation along the solar surface, this simple approximation also provides close results to those produced with the analytic modeling of weak shock waves (Afanasyev & Uralov 2011; Grechnev et al. 2011b). We used the same approximation to fit the expansion of shock-associated CME components as well as the drift rate of type II bursts.
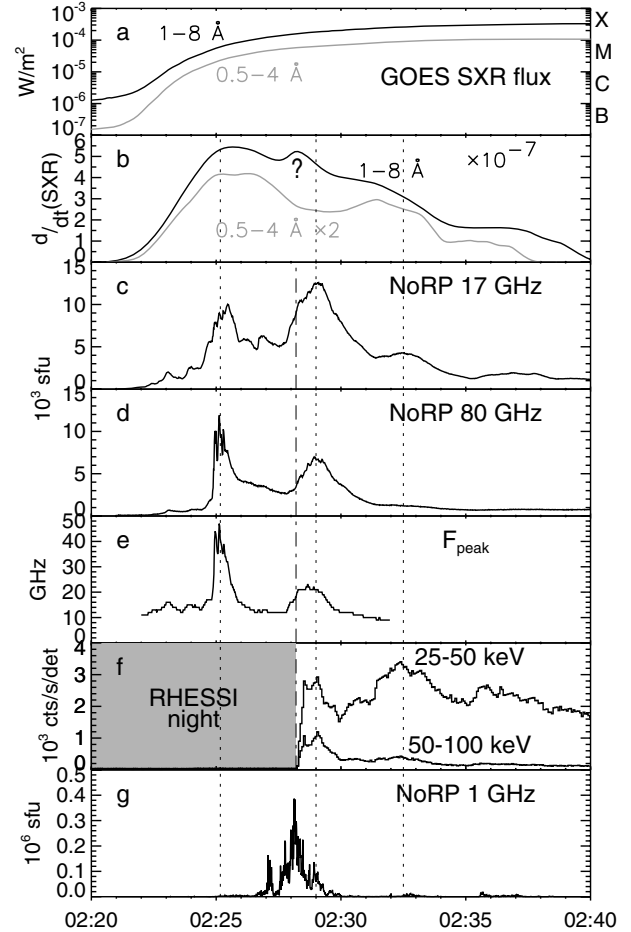

Fig. 1. Time profiles of the event. (a) GOES SXR flux records at 1–8 Å (black) and 0.5–4 Å (gray) and their derivatives (b; the peak indicated by the question mark is probably an artifact); NoRP total flux records at 17 GHz (c), 80 GHz (d), and the microwave peak frequency (e); RHESSI HXR records at 25–50 keV and 50–100 keV (f), and a huge decimetric burst at 1 GHz (g: NoRP). The shaded interval in panel (f) and its dash-dotted continuation indicate RHESSI nighttime. Three vertical dotted lines mark the highest peaks at 17 GHz.

3. Observations

3.1. Time Profiles

Figure 1 characterizes the overall course of the event. The soft X-ray (SXR) flux of the flare reached the X3.4 level (figure 1a). Two major flare peaks at 02:25 and 02:29 are conspicuous at 17 and 80 GHz (figures 1c, 1d). Weaker quasi-periodic peaks with an interval of ~ 5 min, pronounced at lower frequencies, continued afterwards for more than one hour.

Figure 1b shows the derivatives of the two SXR GOES channels (splined 3-sec data). The derivative of the 1–8 Å channel is inconclusive, because a subsidiary peak (the question mark) is most likely an artifact due to the discrete 'staircase' time profile, which started at that time. The second peak at 02:29 is obviously absent in the 0.5–4 Å channel, thus deviating from the Neupert effect (Neupert 1968). This issue is addressed in subsection 4.1.

Figure 1e presents the evolution of the microwave peak (turnover) frequency computed from NoRP total flux data by

using the second-order fit of instant log-log spectra averaged over 1.2 s (see White et al. 2003; Grechnev et al. 2008a). The turnover frequency reaches very high values, exceeding 35 GHz during the first peak and 17 GHz during the second peak. According to expressions of Dulk and Marsh (1982), this fact along with very high flux densities of $> 10^4$ sfu observed at 17 and 80 GHz indicates emission from a very large number of high-energy electrons in the strongest magnetic fields. Flaring during the first peak most likely was stronger and harder than during the second one. The microwave-emitting source was certainly optically thick at both 17 and 34 GHz during the first peak and at 17 GHz during the second peak. However, the turnover frequency of ≤ 20 GHz during the second peak does not guarantee that the 34 GHz source was optically thin at that time (Kundu et al. 2009).

RHESSI missed the first peak and the onset of the second peak due to nighttime (figure 1f). Subsequent evolution of the hard X-ray (HXR) emission in the 25–50 and 50–100 keV ranges shows progressive softening of the HXR spectrum, supporting the assumption that the missed first peak could be still harder.

A huge decimetric burst reached almost half a million sfu at 1 GHz (figure 1g). Its enormous intensity and a sharp spiky time profile indicate an underlying coherent emission mechanism, interpreted by Kintner et al. (2009) as an electron-cyclotron maser (ECM). This burst was only superseded by a burst on December 6 from the same active region 10930. These huge radio bursts caused failures of the GPS and GLONASS navigation systems (Afraimovich et al. 2009a, 2009b; Kintner et al. 2009).

3.2. Eruptions

Eruptions in the 2006 December 13 event were previously considered by Asai et al. (2008) (eruptions EF2 and EF3 in our notation), Sterling et al. (2011) (eruption EF2), and Kusano et al. (2012) (eruption EF1). Nevertheless, their kinematics has not been studied so far. We analyzed the eruptions from SXR Hinode/XRT images. Their motions were measured in the same way as done by Grechnev et al. (2011a, 2014) (see section 2). We firstly measured the positions of the leading edge of each eruptive feature from the images. The measured points were used as starting estimates to find the initial and final velocities. We then endeavored to reproduce the motion of a feature in question by describing its acceleration time profile of a Gaussian shape. The kinematic parameters were adjusted in sequential attempts to follow the motion of a feature in question as closely as possible. The motion of the second eruption was more complex: its acceleration was immediately followed by strong deceleration. We used its acceleration profile as a combination of two Gaussian curves, and adjusted their parameters manually.

Hinode/XRT images reveal three eruptive features following each other. Figure 2 presents the first eruptive feature EF1 (left: direct images, right: image ratios), which was weakly visible as a faint elongated brightening extended East–West. EF1 separated from a bright bundle of loops and moved south in the plane of the sky. As Kusano et al. (2012) showed, the initial position of this eruptive feature coincided with the magnetic polarity inversion (neutral) line, which is highlighted
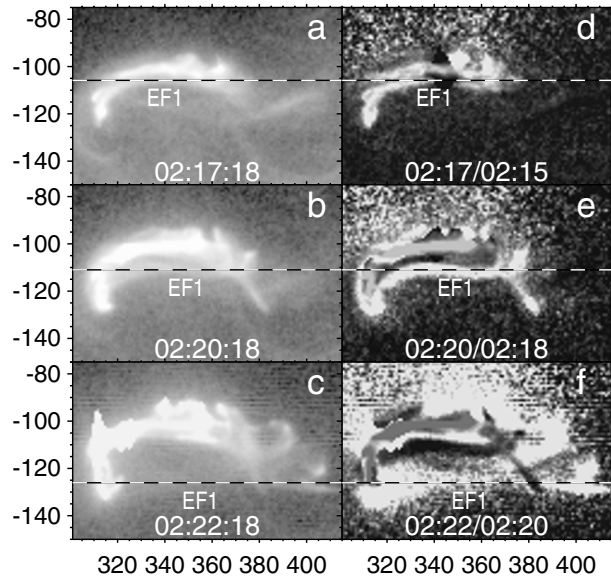

Fig. 2. Hinode/XRT images of eruptive feature EF1: direct images (left column) and image ratios (right column, the times for each pair of the images are indicated in panels d–e). The position of the horizontal dashed line across the southernmost edge of EF1 corresponds to the kinematical measurements presented in figure 3a with the solid curve. The axes show hereafter in similar images arc seconds from the solar disk center.
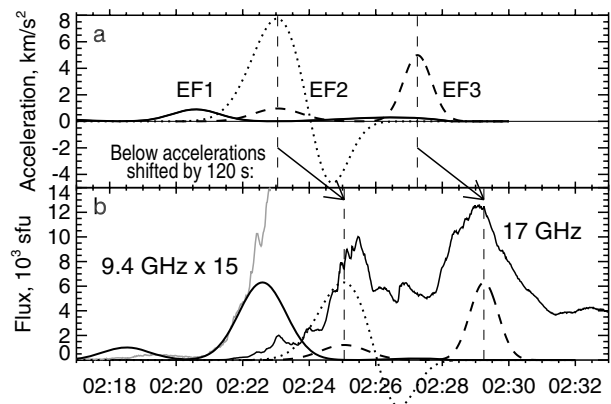

Fig. 3. (a) Measured acceleration plots of eruptive features EF1 (solid), EF2 (dotted), and EF3 (dashed) and (b) microwave time profiles at 9.4 GHz (gray, magnified by a factor of 15) and at 17 GHz (solid) together with delayed normalized acceleration profiles of EF1–EF3. The acceleration plots in panel (b) are delayed by 120 s. The vertical dashed lines denote the acceleration peaks of EF2 and EF3.

in figures 2a–2c by the brightest loop-like bundle arranged along it. The displacement from the initial position of the horizontal dashed line crossing the southernmost bend of EF1 was calculated from the solid acceleration plot in figure 3a. This feature probably was a magnetic flux rope structure, as its initial position along the neutral line implies. The acceleration of EF1 reached in the plane of the sky 1 km s^{-2} at 02:20:30, and its speed reached 110 km s^{-1}, while EF1 was visible.

The second eruptive feature EF2 is shown in figure 4. In the course of expansion, this feature resembled a bow for
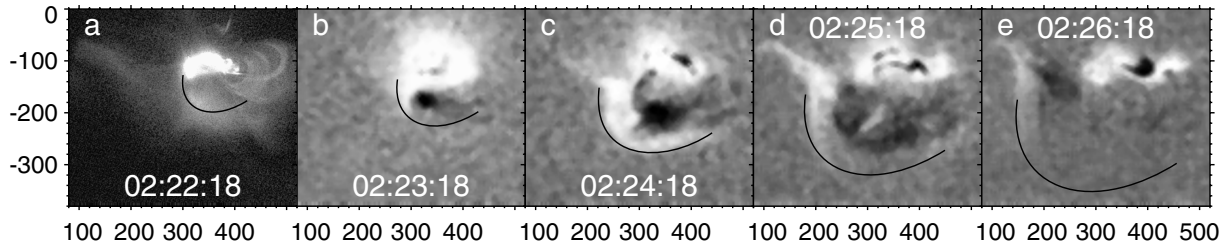
Fig. 4. Hinode/XRT images of the eruptive feature EF2. Panel (a) presents an original image without subtraction. Images in panels (b–e) are running differences. The black ovals outlines the leading upper part of EF2 according to the dotted acceleration plot in figure 3a.

shooting arrows; only its east part is clearly visible. The acceleration plot of EF2 is presented with the dotted curve in figure 3a. EF2 accelerated up to $8\,\mathrm{km\,s^{-2}}$ at 02:23, reached $750\,\mathrm{km\,s^{-1}}$, and then strongly decelerated to $456\,\mathrm{km\,s^{-1}}$. Asai et al. (2008) provided a close estimate of its plane-of-sky speed of $650\,\mathrm{km\,s^{-1}}$. They also revealed a strong blue shift of emission, whose hot ($> 2\,\mathrm{MK}$) source was close to this feature ('BS2' in their notation) based on spectroscopic data of Hinode/EIS at 02:22–02:24. The authors considered EF2 as being a manifestation of an MHD shock wave.

However, the properties of feature EF2 are inconsistent with its wave nature. Sterling et al. (2011) considered feature EF2 as a magnetic loop system pushed outward by some core eruption, so that the initial position of EF2 might have coincided with a static loop in figure 4a. Nevertheless, the excitation of shock waves in this event conjectured by Asai et al. (2008) is undoubted as shown by, e.g., Liu et al. (2008); we will confirm this later.

Before any comparison of the kinematical properties of the eruptive features EF1, EF2, and EF3 with different observational facts, we now try to understand what feature EF2 could be in nature. This eruptive feature was the largest in size and the most impulsive in this event. The eruption resulted in the appearance of the double major regions of coronal dimming on the periphery of AR 10930 (see Imada et al. 2007, 2011; Jin et al. 2009; Attrill et al. 2010). Figure 5 presents the eruption of EF2, the dimming regions, and the SOHO/MDI magnetogram produced at 01:40, shortly before the event. The dimming regions were revealed from a difference of the SOHO/EIT 195 Å images observed after the event and before it. The criterion to select dimming was a brightness decrease by $25\,\mathrm{counts\,pixel^{-1}}$ (the quiet Sun's level was $40\,\mathrm{counts\,pixel^{-1}}$). To eliminate complicating small-scale structural features, both the EIT difference image and the magnetogram were smoothed by convolution with a two-dimensional Gaussian kernel (4 pixels width).

The solid curves in figure 5 outline the clearly visible parts of EF2; the dashed curves outline their possible extensions (cf. figure 4). A comparison of figures 5 and 4 shows that the eastern end of the 'bow' was fixed and located within the large dimming region D1, whose magnetic polarity was positive (figure 5c). Thus, the western end of the bow-like feature EF2 must be rooted in a negative-polarity region. As the outlining curves indicate, the western end of EF2 was most likely located in the dimming region D2 dominated by the negative polarity.

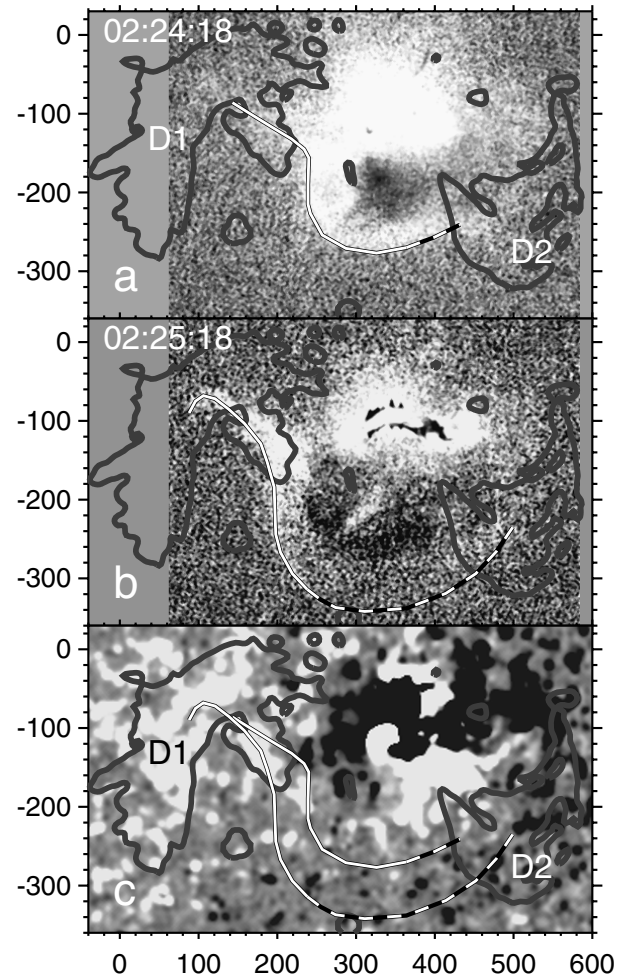In classical 'double dimming' events, coronal dimming

Fig. 5. Two XRT images of the eruptive feature EF2 (a, b) in comparison with double dimming regions D1 and D2 (dark gray contours) and the MDI magnetogram (c). The solid curves outline the parts of EF2 clearly visible in these images. The dashed parts of the curves outline suggestions of EF2 revealed from the XRT images processed in different ways.

regions are considered as opposite-polarity footpoints of the ejected CME's flux rope (Hudson & Webb 1997; Sterling & Hudson 1997; Webb et al. 2000; Mandrini et al. 2005). This concept appears to be consistent with the discussed properties of feature EF2, which was probably an eruptive flux rope, the largest one and most impulsive in this event. The magnetic
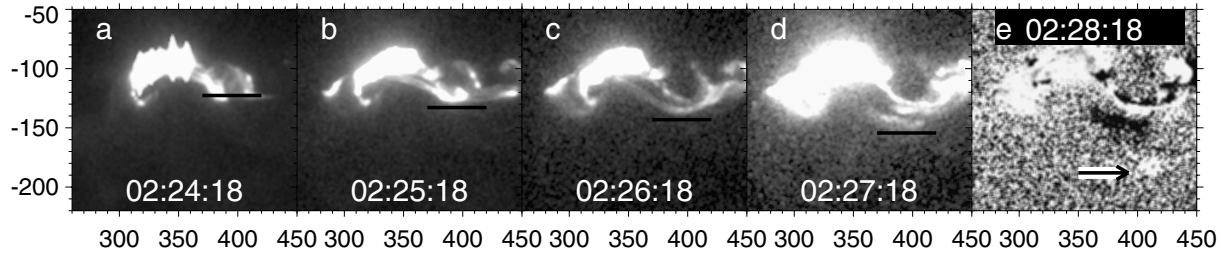
Fig. 6. Hinode/XRT images of the eruptive feature EF3. Panels (a–d) present non-subtracted images, and panel (e) shows a difference image. The black bars in panels (a–d) mark the farthest bend of EF3 according to the dashed acceleration plot in figure 3a. The black arrow in panel (e) points at a faint latest manifestation of EF3.

fields enveloping the progenitor of the flux rope from above in the strongest-field part of AR 10930 were directed northward, and the axial field was directed westward, as figure 5c shows. This arrangement of the magnetic polarities agrees with the left handedness of the active region indicated by its mirrored-S-shaped configuration and the negative helicity of the corresponding near-Earth magnetic cloud (Liu et al. 2008).

The progression of reconnection caused by the eruption formed the flare arcade, whose development involved the strongest magnetic fields between the sunspots. The process seems to be well described by the standard flare model. A seemingly contradiction with the conclusion of Sterling et al. (2011) about the major eruption away from strong fields (their figures 6, 8, and 9) is reconciled in subsection 3.6.

The second eruptive episode probably inspired eruption of the third feature, EF3, presented in figure 6. Its acceleration plot is shown by a dashed curve in figure 3a. Feature EF3 was initially located along the neutral line; probably, it was also a flux rope. EF3 underwent two acceleration episodes. The first, a weaker one, occurred simultaneously with the acceleration of EF2 at 02:23. This determined its appearance simultaneously with the first microwave peak. The maximum acceleration of EF3 reached $5 \, \mathrm{km \, s^{-2}}$ at 02:27 with a final speed of $420 \, \mathrm{km \, s^{-1}}$. Asai et al. (2008) also revealed a strong blue shift for this feature (BS1 in their notation), and interpreted it as an ejected plasmoid. The plane-of-sky speed estimated by the authors, $90 \, \mathrm{km \, s^{-1}}$, was less than our measurements show (probably due to difficulties to reveal its faint latest manifestation at 02:28:18 in figure 6e), while its line-of-sight speed of $240–280 \, \mathrm{km \, s^{-1}}$, estimated by Asai et al. (2008), seems to agree with our result.

From the fact that the appearance of EF3 corresponded to the first microwave peak recorded with NoRP, Asai et al. (2008) reasonably concluded that the flare was a product of magnetic reconnection induced by the eruption. Comparisons of the detailed acceleration plots for eruptive features EF1, EF2, and EF3 in figure 3a with microwave bursts in figure 3b reveal a relation between them, which appears to be still more impressive.

Figure 3b presents microwave time profiles at 17 GHz (black solid) and at 9.4 GHz (gray, a magnified initial part) along with normalized acceleration plots from figure 3a, shown with the same line styles, and arbitrarily shifted by 2 min later. The early rise of the 9.4 GHz emission coincides with the delayed acceleration of EF1, and the 17 GHz time profile exhibits
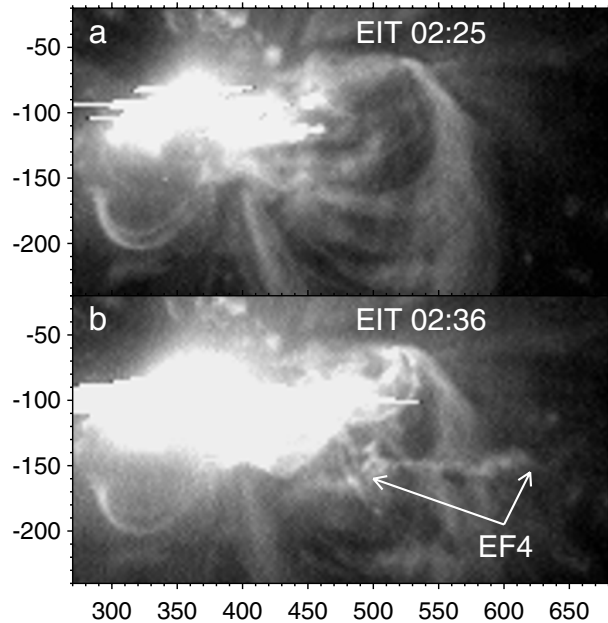

Fig. 7. Eruptive feature EF4 in EIT 195 Å image at 02:36 indicated by the arrows (b). EF4 is certainly absent in the preceding EIT 195 Å image at 02:25.

a striking similarity with the delayed acceleration curves of EF2 and EF3. Thus, the flare bursts were caused by the eruptions, and not vice versa. Each eruption was apparently causally related with another, and preceded a flare burst.

This relation is consistent with the standard flare model, especially in its modern form. Kusano et al. (2012) numerically simulated MHD processes caused by a wide variety of magnetic structures, and compared the results with Hinode imaging data. According to their conclusion, the trigger of the 2006 December 13 flare was manifested in the eruption of EF1; this is consistent with the measured temporal relation between the acceleration of EF1 and the microwave flare emission presented in our figure 3.

Eruption EF3 was not the last one in this event. Figure 7b presents one more eruptive feature, EF4, in a SOHO/EIT 195 Å image mentioned by Asai et al. (2008). The position of this feature at 02:36 rules out its identity with any of the preceding ones. This feature is not visible in either Hinode/XRT images (probably its temperature was lower than XRT can see) or

GOES-12/SXI ones. It is not possible to measure its motion from a single image. Assuming that its relation to microwaves was approximately the same as for the preceding eruptions, one might assume the onset of its motion at the early rise of the next microwave peak, marked by the dotted line in figure 1 (02:32:30), or about 2 min before, i.e., at 02:29–02:31. The initial position of EF4 might be marked by the westernmost loops in XRT images and ribbons in SOT ones in figure 9. With this assumption, the plane-of-sky speed of its leading edge should be 250–400 km s^{-1}, which seems to be reasonable. Thus, association of the eruptive feature EF4 with the next, smaller flare peak at 02:32:30 is possible.

The time profiles of accelerations in figure 3 had a quasi-periodic character. The eruption of EF4 probably followed this trend. We remind that the quasi-periodic pulsations continued long afterwards in microwaves. This circumstance induces thinking about possible causes of the oscillatory behavior of this event and the role of the oscillations in triggering the eruptions. However, this issue is beyond our scope.

3.3. Development of the Flare

3.3.1. Pre-flare emission

Smolkov et al. (2009) have shown that microwave emission of active region 10930 at 17 GHz under relatively quiet conditions during a week before the December 13 flare was dominated by a neutral line source (NLS). Such long-lived sources reside in the vicinity of the main neutral line where the horizontal magnetic component is maximum (Uralov et al. 2006). Emission of a NLS at 17 GHz is dominated by either the top of footpoints of a low-lying bundle of loop-like structures rooted in strong magnetic fields of sunspots. Such microwave sources are due to gyroresonance emission at the fourth, or even third, harmonic of the gyrofrequency; i.e., the magnetic field strength in the corona reaches 1500–2000 G at a place where a NLS resides (Uralov et al. 2006, 2008; Nita et al. 2011). Thus, the existence of a NLS in AR 10930 indicates a very strong magnetic field in the corona. Such sources are only observed in active regions that produce GOES X class flares.

The NLS had a brightness temperature of 0.3–0.5 MK. It was located above the neutral line, approximately in the middle between the main sunspots of opposite polarities, where the eruptive feature EF1 originated. On December 12, the NLS shifted to the larger northern sunspot of S-polarity, and persisted there until the flare onset (and reappeared after the flare). The flare started close to the position of the NLS, or exactly there. This situation appears to be a typical one (Uralov et al. 2008).

3.3.2. Flare rise

When the flare started, the major microwave emission was contributed by gyrosynchrotron from high-energy electrons. Before considering the flare course in microwave images, we recall that the turnover frequency of the microwave spectrum in figure 1e reached 47 GHz during the first peak. Thus, the microwave source at that time was certainly optically thick at both operating frequencies of NoRH 17 and 34 GHz. We therefore limit our analysis with only the consideration of 17 GHz emission, and take advantage of polarization data available at 17 GHz.

To produce images at 17 GHz, we used the Fujiki program for the rise phase of the flare. Very bright microwave sources during the peaks considerably exceeded 100 MK, which makes impossible usage of standard imaging software of NoRH. Therefore, after 02:24 we used a program developed by H. Koshiishi for imaging extreme flares. Calibration of the images in brightness temperatures was performed by referring to total fluxes recorded with NoRP, as proposed by K. Shibasaki.

One of the major difficulties in analyses of microwave images, along with those produced in different spectral domains, is their accurate coalignment, because NoRH does not provide an absolute pointing. We overcome this problem by comparing the NoRH images with the flare ribbons shown by Hinode/SOT in the Ca H-line, and by comparing the polarized microwave emission (Stokes V component) with the magnetograms of Hinode/SOT and SOHO/MDI, as shown in figure 8. We have Hinode magnetograms produced several hours before the event, at 20:30 on December 12, and after the event, at 04:30 on December 13. The southern N-polarity sunspot rapidly changed at that time. There is a SOHO/MDI magnetogram produced at 01:40, close to the onset of the event, but the large stronger northern S-polarity sunspot, which was rather stable, is heavily distorted in the magnetogram due to 'high-field saturation'. We combined contours of the stable negative sunspot taken from the Hinode magnetogram with contours of the variable positive sunspot from the temporally close MDI magnetogram, which was not distorted. The two magnetograms were accurately coaligned with each other, and referred to the pointing of MDI in figure 8.

The gray-scale background in figure 8a presents a NoRH 17 GHz image in total intensity (Stokes I) observed at 02:24, i.e., at the rise phase of the first peak. The solid white contours outline the levels of $[-3000, -1500]$ G in the Hinode/SOT magnetogram. The solid black-on-white contour outlines the $+1500$ G level in the SOHO/MDI magnetogram. The broken contours correspond to 50% levels of the polarized emission at 17 GHz (dashed positive, dotted negative). The polarization at 17 GHz corresponds to the x-mode emission with a degree up to $> 30\%$ at 02:24. The ellipse in the upper-right corner presents a half-magnitude contour of the NoRH beam. Compared with the microwave Stokes I and V data, it shows that the source in total intensity was well resolved and rather large, while the polarized sources were more compact. The negatively polarized region was somewhat extended in the east-west direction.

The peak frequency in figure 1e indicates that the 17 GHz source at that time approached the optically thick regime. Thus, the major emission in total intensity should be radiated from upper layers of the source, where the magnetic fields were weaker (see Dulk & Marsh 1982; White et al. 2003; Kundu et al. 2009). The positions of the emitting regions in figure 8b correspond to the above considerations. The solid white contours here outline the levels of [25, 50, 100] MK in the total intensity at 17 GHz, while the maximum brightness temperature over the image is 128 MK. The broken contours show the same 50% levels of the polarization as in the upper panel.

Overall, figure 8 shows that the total intensity at 17 GHz was mainly emitted from the broad upper part of the flare
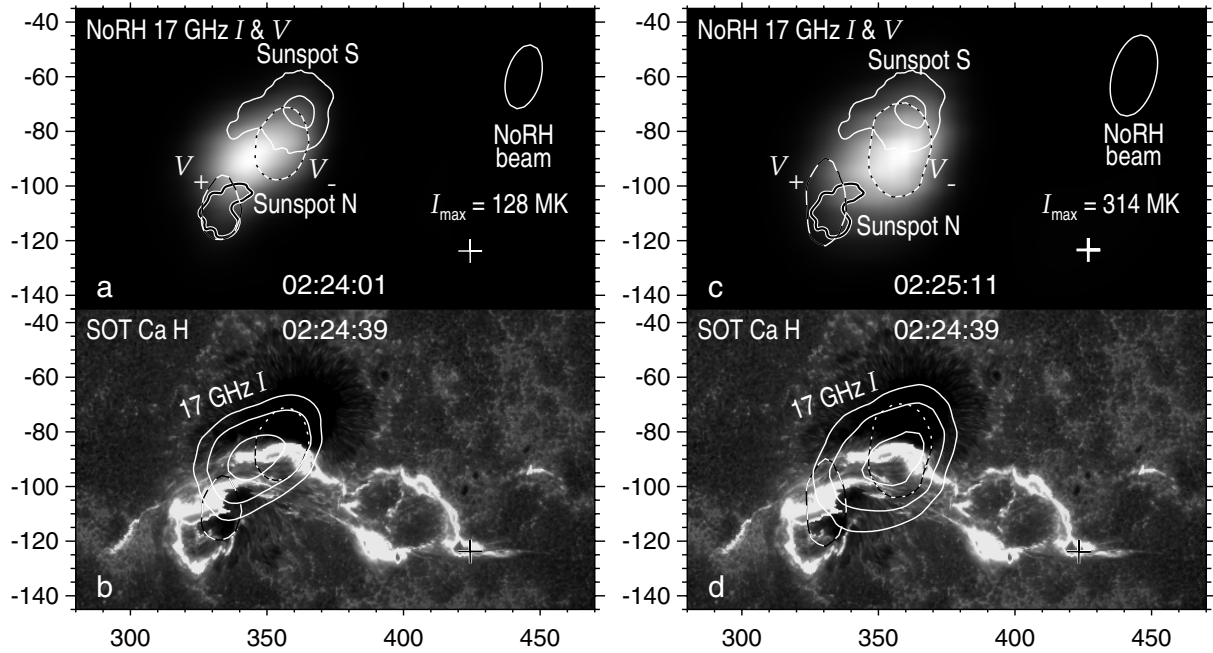
Fig. 8. NoRH and Ca H (SOT) images during the rise phase (a,b) and at the first peak (c,d). The contour levels for the 17 GHz intensity are [25, 50, 100] MK (a) and [62, 125, 250] MK (b). The contour levels of the polarized component (Stokes V) are 50% of both positive (dashed) and negative (dotted) maxima. The white contours in panels (a,c) outline the S-sunspot in the Hinode/SOT magnetogram, and the black-on-white contours outline the N-sunspot in the SOHO/MDI magnetogram (the levels are [−3000, −1500, +1500] G). The crosses mark the brightness center of the weaker west microwave source and the corresponding position in the SOT image.

arcade, whose bases are highlighted by the ribbons in the SOT Ca H-line image. The polarized regions correspond to the conjugate legs of the arcade loops. The optical thicknesses of the polarized regions, viewed slightly aside from the arcade top, were most likely less than that of the broad cover source. Microwaves were mostly emitted by the portion of the arcade between the sunspots where the magnetic field was much stronger than sidewards and, probably, the number of high-energy electrons was also larger.

Nevertheless, microwave images show a suggestion of an additional weak source moving west from the major flare site during 02:22–02:25. This presumable source overlaps with a region of strong side lobes from the major source. The reality of this secondary source is supported by its larger size, gradual shape, and progressive motion west, all of which are different from the side lobes. We have roughly measured probable positions of the brightness centers of the secondary source manually, and plotted them with the white crosses in figures 8 and 9. The crosses approximately correspond to the expanding western portions of the ribbons in the SOT and XRT images. Thus, the weak microwave source moving west displays the development of the flare arcade westward in weaker magnetic fields, apparently caused by the eruptions. On the other hand, the closeness of its measured positions to the developing ribbons indicates that the coalignment accuracy of all the images is satisfactory. Its uncertainty presumably does not exceed 5″.

3.3.3. First flare peak

Figures 8c, 8d present the same set of images as in figures 8a, 8b, but the NoRH 17 GHz data correspond to the first major

peak of the flare (02:25:11). As the very high turnover frequency in figure 1e shows, the microwave source at that time was certainly dominated by optically thick emission, both at 17 and 34 GHz. The maximum brightness temperature at 17 GHz reached 314 MK. Nevertheless, the microwave configuration has not considerably changed. The optically thick part of the microwave source appears to have broadened, as suggested by a decreased degree of polarization of < 15% remaining at the upper part of the flare arcade.

The very high turnover frequency of the microwave spectrum at that time indicates emission from a very large number of high-energy electrons in very strong magnetic fields (see Dulk & Marsh 1982; White et al. 2003; Grechnev et al. 2008a). The constancy of the position of the microwave source, while f_{peak} drastically increased, suggests that the magnetic field strength remained nearly the same. Thus, the major reason for the change could be plentiful ejection of high-energy electrons that should shift the gyrosynchrotron spectrum right, to considerably higher frequencies. Note that this flare peak was apparently caused by the eruption (see figure 3). To find out what could be a reason for such a strong energy release during the first flare peak, we consider the overall course of the flare shown by microwave images along with Hinode/SOT and XRT images.

3.3.4. Overall progression of the flare

The overall course of the flare can be followed from figure 9, which shows selected microwave images (colored shading in two middle rows) along with available XRT (l–p) and SOT (q–u, lower row) images, compared with the NoRP time profile at 17 GHz (a, top row). XRT images were produced every
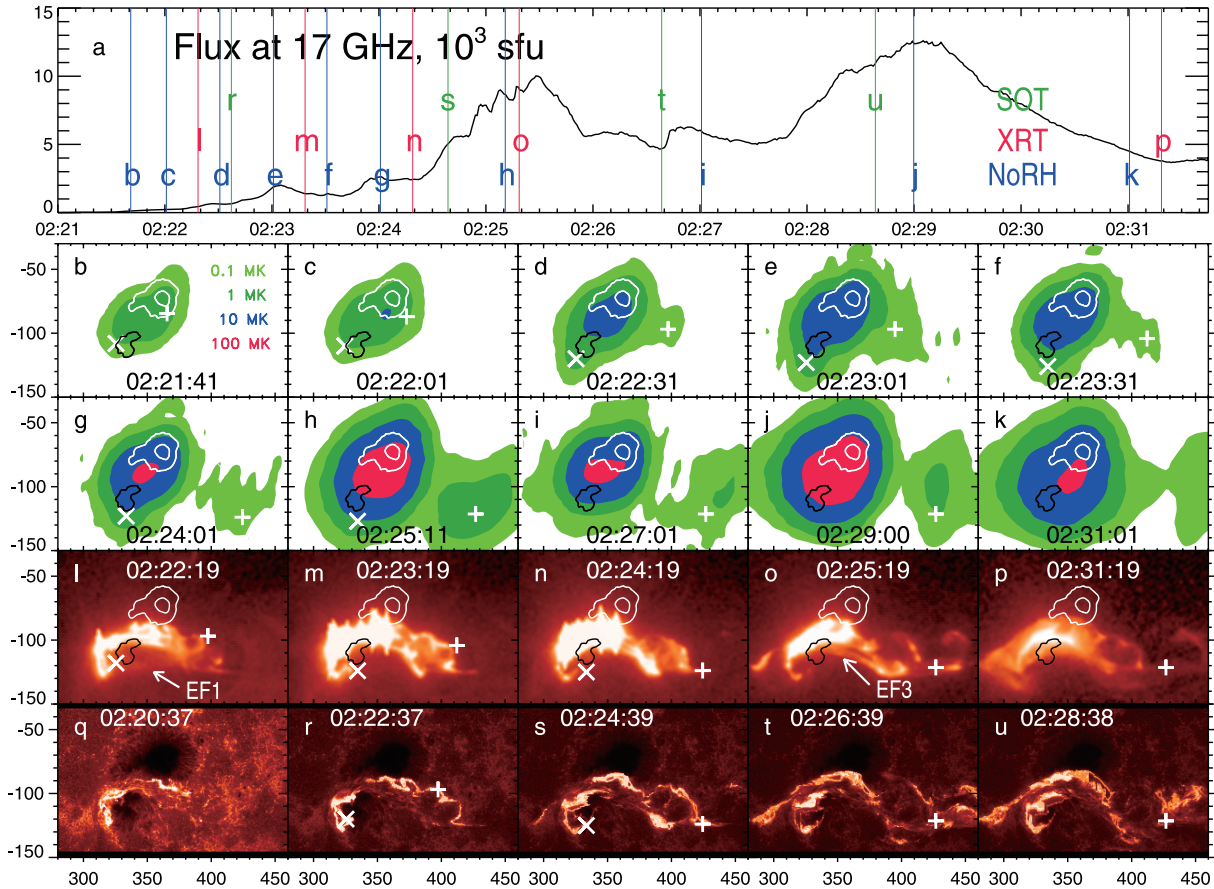
Fig. 9. Overall course of the flare. (a) Total flux time profile at 17 GHz, (b–k) color contours of NoRH 17 GHz images at [0.1, 1, 10, 100] MK, (l–p) Hinode/XRT SXR images, (q–u) Hinode/SOT Ca H-line images. The contours on top of the NoRH and XRT images outline the magnetic N-polarity (black, +1500 G) and S-polarity (white, [−3000, −1500] G). The color vertical lines in panel (a) mark the observing times of the images. The straight and slanted crosses mark the brightness centers of weaker microwave sources and corresponding positions in the XRT and SOT images. Eruptive features EF1 and EF3 are denoted in panels (l) and (o), respectively; their middle parts are indicated by the arrows. Eruptive features EF2 and EF4 are beyond the small field of view presented in the figure.

minute, while only one SOT image in the Ca H-line in two minutes is available. The interval shown in the figure starts from the rise phase, and covers the two major peaks. The colored shading quantifies the brightness temperatures in the 17 GHz Stokes I images from 0.1 MK to 100 MK (see panel b). The white and black contours show again the magnetic field strengths (white [−3000, −1500] G, black +1500 G). The straight white crosses present rough measurements of the weaker 17 GHz source moving westward. The slanted crosses present analogous measurements of the weak southeast-to-south extension of the 17 GHz source. The imaging times are indicated with the vertical lines in the top panel.

The main 17 GHz source persisted between the sunspots being associated with the upper parts of the arcade loops. Although the displayed range of brightness temperatures exceeds the nominal dynamic range of the NoRH, comparison with the XRT and SOT images confirms suggestions of lower-temperature shading and crosses in the NoRH images. During the rise phase, the south flare ribbon developed and moved west, toward the N-sunspot in all of the images. The first major peak occurred when the south ribbon covered the N-sunspot. Changes in the S-sunspot were not as conspicuous,

because the magnetic flux in this sunspot was much larger than that in the N-sunspot.

The observations confirm the strong dependence of the energy release rate in a flare on the magnetic field strength expected from the standard flare model. This circumstance was demonstrated by Asai et al. (2002, 2004). Extreme parameters of sunspot-associated flares were shown by Grechnev et al. (2008a) and Kundu et al. (2009). Among these properties are strong hard X-ray and gamma-ray emissions and high SEP productivity.

After the first major peak, the magnetic flux associated with strong fields of the N-sunspot mostly reconnected. The microwave emission did not exceed 150 MK by 02:28. Then, the next eruption caused one more pulse of strong energy release and injection of accelerated electrons into the flare region. The microwave peak frequency increased to ≈ 20 GHz (figure 1e), and the most 17 GHz source became optically thick again. The brightness temperature at 02:29 reached a still higher value of 378 MK, possibly due to expansion of the microwave-emitting region upward into weaker magnetic fields. Though this peak was higher at 17 GHz than the first one, the energy-release rate and the number of high-energy

electrons were probably less strong.

One of distinctive features of this extreme flare was the increase of the microwave peak frequency well above 17 GHz, and even above 34 GHz during the first peak. Unlike a typical situation, the microwave-emitting source certainly was not optically thin at 17 GHz during the main peaks. This could also be true even with a lower peak frequency [see Kundu et al. (2009) for detail]. These facts can shed light on features of the spectral evolution of the flare emissions in this event (see, e.g., Ning 2008). The reason for these extreme properties was the involvement in reconnection processes of the strongest magnetic fields rooted in the sunspots in accordance with the conclusion of Jing et al. (2008).

3.4. EUV Shock Signatures

As shown in the preceding sections, at least two impulsive eruptions with very strong acceleration of $> 15\,g_\odot$ ($g_\odot$ is the solar gravity acceleration) occurred in the event. As explained in section 1, coronal shock waves must have been excited by these impulsive pistons. The cartoon in figure 10 outlines a conception of the front shape and the velocity of a coronal wave excited in an active region (AR). The positions of the wave front in the corona at three different times (t_1, t_2, and t_3) are illustrated with the dotted curves, and their corresponding near-surface traces are shown with the solid ellipses. The arrow **grad** $V_{\rm fast}$ represents the conditions in the low corona above the active region, favoring wave amplification and the formation of a discontinuity at t_1. The blast-like wave is expelled from the AR's magnetosphere into regions of weaker magnetic fields. The shape of the wave front in the low corona is determined by the Alfvén-speed distribution. The front shape is close to an oval, possibly oblate in its upper part with a moderate intensity of the wave. The center of the oval progressively displaces upward, as increasing slanted crosses show. If the shock wave is strong enough, then the shape of its front should be an oval expanded in its upper part. Crossing by the shock front of the current sheet inside a coronal streamer excites type II radio emission.

Probable signatures of shock waves are large-scale transients in extreme ultraviolet (EUV), known as 'EUV waves' (or 'EIT waves'). Such a transient was really present in this event (see, e.g., Asai et al. 2008; Liu et al. 2008, 2009; Attrill et al. 2010; Nitta et al. 2012). However, no analysis of this transient was carried out besides a conclusion about the association of this 'EUV wave' with a shock.

The routine imaging rate of SOHO/EIT of 12 min was insufficient to study the propagation of such transients in detail. We therefore combine EIT observations with those of GOES-12/SXI, although its images reveal 'EUV waves' poorer than EIT, and heavily suffer from the scattered light. To understand what the images show, we calculated the expected propagation of a shock wave over the spherical solar surface, assuming a homogeneous corona in the way described in section 2, and compared the calculated positions of the front with its presumable traces in real images. We used as input the parameters probable excitation times of shocks corresponding to the peaks of acceleration of EF2 and EF3 and one of the well-defined wave fronts. We then attempted to find other signatures of the shock propagation, and corrected
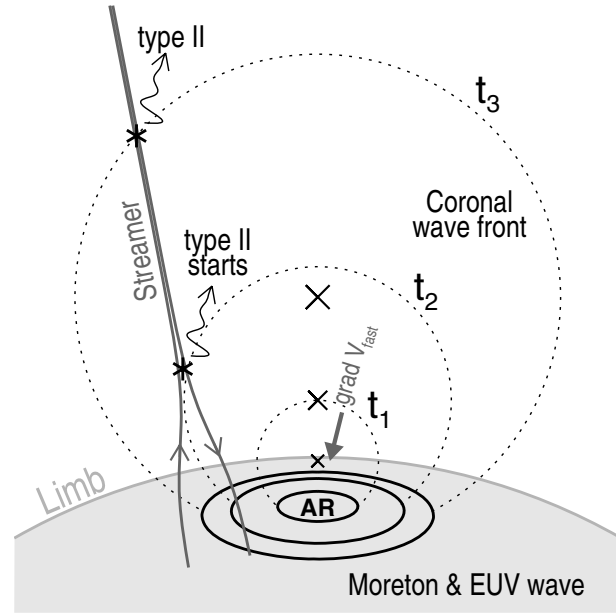

Fig. 10. Fast magnetosonic shock wave excited by an impulsive eruption in an active region (AR).

the input parameters to fit them better.

Attempts to fit in this way the observed shock signatures as the propagation of a single front have resulted in discrepancies with the observations. The calculations could be reconciled with real images when we considered two shock fronts to be following each other. One shock (shock 1) was excited by eruption EF2 at 02:23, and the second one (shock 2) was excited by eruption EF3 at 02:27. The results are shown in figure 11.

Figure 11a shows an EIT 195 Å pre-event image followed by a set of EIT and SXI running-difference ratios in panels (b–i). The initial position of the wave center is marked by the slanted cross. The pre-event image reveals some inhomogeneities in the corona that can affect the propagation of a shock wave. One of them is a darker region CH northwest from the active region, resembling a coronal hole. A SOHO/MDI magnetogram shows in this region an enhanced, predominantly unipolar (negative) magnetic field. Thus, the Alfvén speed was enhanced above this region. Other inhomogeneities are plage regions PR east from AR 10930 and a coronal hole farther eastward.

The white and black ellipses present intersections of two spheroidal wave fronts with the spherical solar surface calculated for wave propagation in a homogeneous medium. This simplified approximation is only convenient for a portion of the wave front running along the homogeneous solar surface. The ellipses were calculated by referring to obvious wave traces in a few images. On the other hand, the ellipses hint at shock suggestions in other images, some of which are indicated by the arrows. For example, the northwest brightening marked by the arrows in figures 11b, 11c might be due to scattered light; however, its expansion corresponds to the expected propagation of the second shock front. Also, the dark patches in these running-difference ratios (figures 11b, 11c), preceded by faint brightenings, might be due to a propagating disturbance. Thus, if some of the mentioned features visible in the GOES/SXI
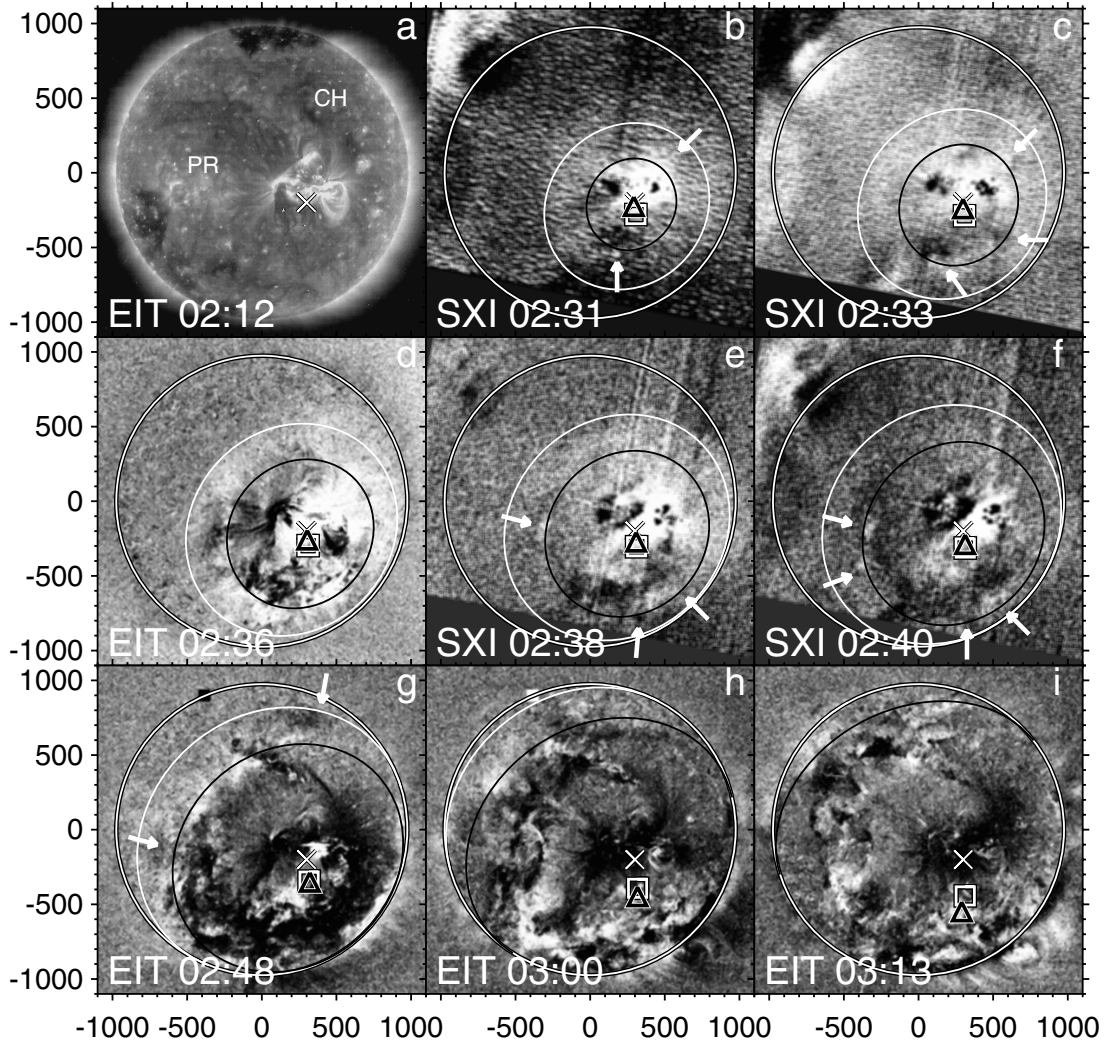
Fig. 11. EUV traces of two shock waves in SOHO/EIT and GOES-12/SXI images. (a) Pre-event EIT 195 Å image. 'CH' is a coronal hole; 'PR' is a plage region. The slanted cross shows in all images the initial position of the wave center. (b–i) Running-difference ratios of EIT 195 Å (d, g, h, i) and SXI (b, c, e, f) images. The ellipses present the calculated intersections of the spheroidal shock fronts with the spherical solar surface (white shock 1, black shock 2). The arrows indicate suggestions of shock traces. The white squares mark the current epicenters of shock 1. The black triangles mark the current epicenters of shock 2.

images are real, then their positions correspond to expected traces of the shocks.

The two fronts are especially pronounced in figure 11d. The compact east brightenings, indicated by the arrows in figures 11e and 11f, might be due to the passage of a shock front over the west plage region. The north dark patch just behind the white ellipse, indicated by the arrow in figure 11g, certifies the passage of a disturbance there. Similarly, traces of the disturbance are visible behind the calculated front of the first shock in figures 11h, 11i.

The actual fronts ran faster than the calculated ellipses in the northwest region CH with a higher Alfvén speed. This deviation is expected for a shock front. The plage regions PR, and a coronal hole eastward, also affected the propagation of the shocks. Remarkable is a progressive displacement of the wave epicenters (the squares and triangles) toward the southern polar coronal hole. We had to introduce this displacement to

co-ordinate the calculated ellipses with actual large-scale shapes of the fronts. The progressive shift is a property of 3D fast-mode MHD shock waves, whose propagation is determined by the Alfvén-speed distribution (figure 10; Grechnev et al. 2011a, 2011b; Afanasyev & Uralov 2011).

To our knowledge, this is the first case of two shocks following each other along the solar surface with a difference between their excitation times as small as four minutes, revealed from imaging observations. The detection of the two separate shock fronts became possible presumably because the first shock was considerably faster than the trailing one.

Figure 12 presents kinematical plots for the propagation of the two shock fronts along the spherical solar surface corresponding to the ellipses in figure 11. To facilitate a comparison of the plots with the images, the vertical dashed lines mark the times of the EIT images shown in figure 11. The labels 'd, g, h, i' in figure 12a indicate the corresponding panels
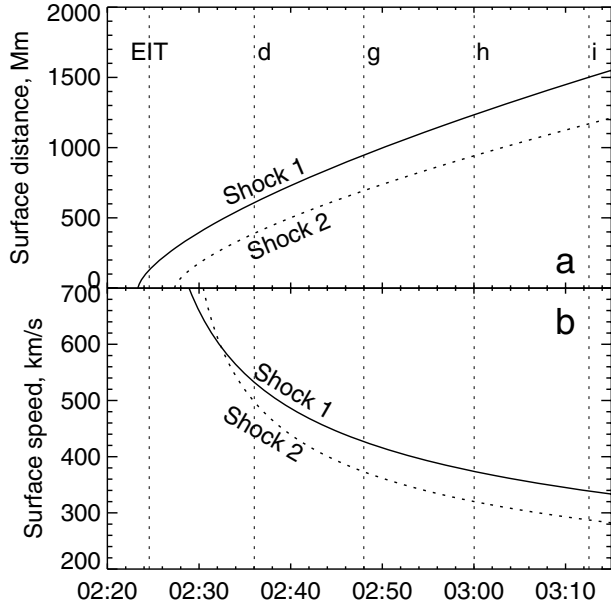
Fig. 12. Distance-time (a) and velocity-time (b) plots of the two shocks following each other along the solar surface. The distances are measured from the initial wave center (the slanted cross in figure 11). The onset times are 02:23:20 for shock 1 and 02:27:20 for shock 2; $\delta = 2.0$ for both shocks. The vertical dotted lines mark the imaging times of EIT, and the labels denote the corresponding panels in figure 11.

Fig. 13. Dynamic radio spectrum composed from Culgoora, Learmonth, and Callisto/SSRT data (b) in comparison with the microwave time profile at 17 GHz (NoRP). Presumable onset times of shock 1 (02:23:20) and shock 2 (02:27:20) are denoted by the vertical broken lines in the top panel. Some type II bands detectable in the spectrum are outlined with black curves calculated for the expected shock propagation. The solid and dotted pairs of curves outline signatures of shock 1, and the dashed one outlines shock 2. The dashed white ovals indicate the most pronounced harmonic pairs of type II bands.

in figure 11. Both shock fronts were monotonically decelerated. Asai et al. (2008) estimated the speed of the "EIT wave" to be "*570 ± 150 km s⁻¹ in the southeast direction*," probably relating the estimate to 02:36. We remind that the shock fronts in figure 11 were calculated for isotropic shock propagation along the surface, and therefore the plots in figure 12 represent an azimuthally-averaged kinematics of the wave fronts.

The average propagation velocities of the first and second EUV wave's fronts at a distance of $1\,R_\odot$ from their epicenters in the active region were about 500 and $380\,\mathrm{km\,s^{-1}}$, respectively. Typical propagation velocities of 'EUV waves' at such distances are close to the fast-mode speed in the low corona above the quiet Sun and, most likely rarely exceed $300\,\mathrm{km\,s^{-1}}$ (Mann et al. 2003; Grechnev et al. 2011b). Such high propagation velocities in the 2006 December 13 event are evidence of a nonlinear character of the near-surface magnetosonic wave and a high probability of its shock-wave regime. However, the supersonic propagation velocity of the visible wave disturbance does not guarantee that the observed plasma compression moves together with the shock front. The top of a nonlinear wave moves faster than its foot, even before the formation of the discontinuity. To reveal a velocity jump evidencing a shock front, one should directly measure the kinematics of magnetic structures (e.g., coronal loops) after passage through them of the near-surface "EUV wave." The observational data do not allow such direct measurements. To obtain further support for the shock-wave regime of the wave front, we consider in the next section its portion responsible for the appearance of the type II emission, which is believed to be due to a shock front.
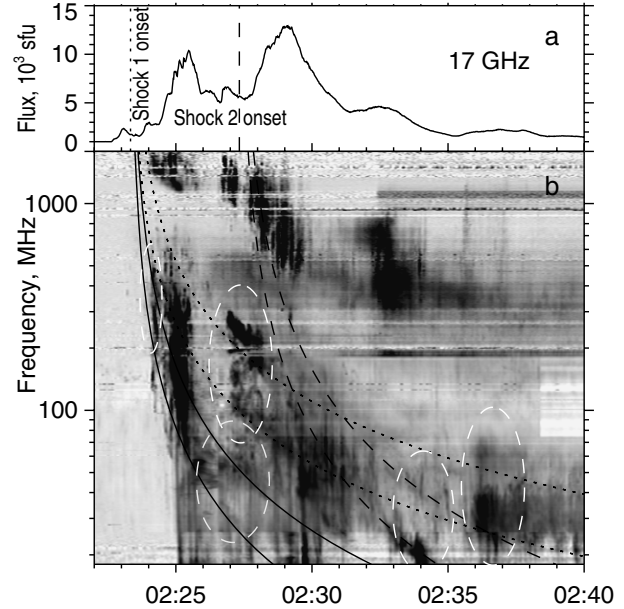
3.5. Dynamic Radio Spectrum

As mentioned, radio emission caused by the 2006 December 13 event was extraordinarily strong in the meter waverange and especially in the decimeter one, and especially decimeters, with total fluxes of up to 0.5×10^6 sfu (figure 1g). The huge decimetric burst was apparently due to a coherent mechanism, probably ECM (Kintner et al. 2009). This coherent emission complicates the consideration of weaker type II and type IV bursts. The long-wave part of the type II burst was discussed by Firoz et al. (2011, 2012), and analyzed up to kilometers by Liu et al. (2008).

The short-wave portion of the type II and type IV bursts is most important for our analysis. To cover the whole frequency range of interest, and make the dynamic spectrum clearer, we combined the data of Culgoora, Learmonth, and Callisto/SSRT spectrometers. The composite spectrum is presented in figure 13b in comparison with the microwave total flux at 17 GHz in figure 13a.

The dynamic spectrum shows probable manifestations of type III, II, and IV bursts. A few strong trains of coherent emission (presumably ECM) correspond to the microwave peaks in figure 13a. A drifting type IV burst masked by stronger coherent bursts suggests emission from electrons trapped in an expanding flux rope of the developing CME. A detailed analysis of the type IV emission requires the involvement of longer-wave data, which is beyond our scope.

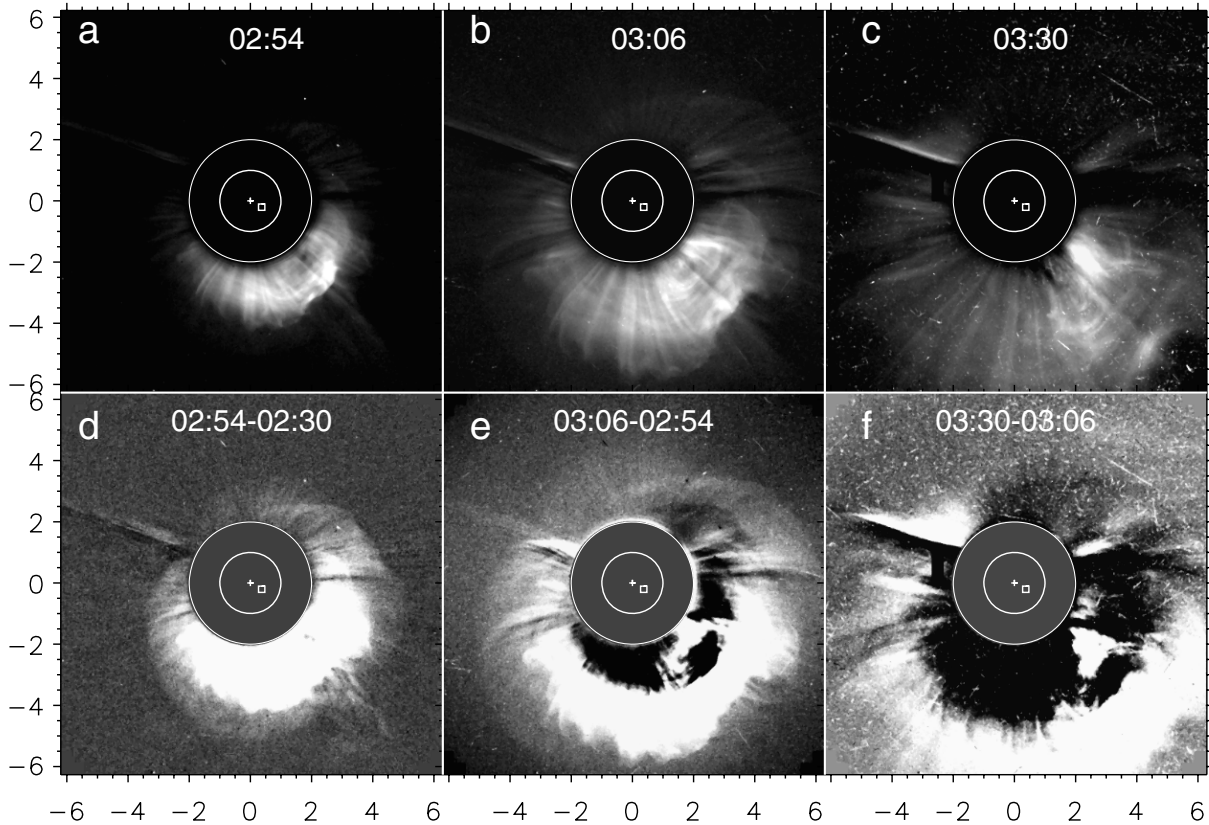The structure of the type II burst is complex, suggesting

Fig. 14. LASCO/C2 images of the CME developed in the 2006 December 13 event. Top row (a–c): fixed-base ratios present the structure of the CME. Bottom row (d–f): enhanced-contrast running differences reveal faint features associated with a leading edge presumable formed by the shock front. Apparent inner features in the running-difference images are due to the subtraction of preceding images, and can be deceptive. The inner circle denotes the solar limb, and the outer one denotes the internal boundary of the C2 field of view ($2\,R_\odot$). The cross marks the solar disk center. The square marks AR 10930. The axes show the distances from the solar disk center in solar radii.

emissions from different coronal streamers stressed by two shock fronts (see figure 10 and Grechnev et al. 2011a for details). Some well-pronounced pairs of type II bands are indicated in the figure by white dashed ovals. To identify these manifestations with a particular shock, and follow the drift rate for each of them, we used the power-law approximation of shock-wave propagation (see section 2 and Grechnev et al. 2011a, 2011b). To recognize the signatures of the shocks in the dynamic spectrum, we firstly analyzed the spectra of Culgoora, Learmonth, Callisto/SSRT, and HiRAS separately, and then verified the results by comparing them with each spectrum.

The results that we have reached so far are presented in figure 13b with the black pairs of curves (fundamental & second harmonic). The solid and dotted pairs of curves outline the signatures of shock 1, whose presumable onset time of 02:23:20 is denoted by the dotted line in figure 13a. These two pairs of bands were presumably generated by two parts of the shock 1 front passing in two different streamers. Similarly, all of the dashed lines are related to shock 2 with an onset time of 02:27:20. The onset times have actually been estimated in attempts to achieve the best correspondence of the outlining curves with the actual signatures of the shocks in the dynamic spectrum, and used afterwards in outlining the shock traces in figure 11. The kinematical curves of the near-surface "EUV waves" in figure 12, on one hand, and

the outlining curves corresponding to the coronal shocks in figure 13, on the other hand, were obtained in self-consistent calculations to fit both EUV-imaging and radio data. This fact confirms that both coronal waves were shock waves, at least as early as the corresponding type II bursts started. Their onset times were about 02:24 for the first-wave bands and 02:33 for the second-wave ones.

The outlining curves presented in figure 13b were calculated for shock waves, which were impulsively generated and freely propagated afterwards. While the shocks were most likely excited by the impulsive-piston mechanism, their further behavior resembles decelerating blast waves.

3.6. CME

The 2006 December 13 event produced a rapidly decelerating halo CME with an estimated average speed of $1774\,\mathrm{km\,s^{-1}}$ according to the SOHO LASCO CME Catalog[1] (Yashiro et al. 2004). The CME is shown in figure 14 in two representations approximately corresponding to their appearance in the Catalog. The top row (a–c) contains fixed-ratio images, which allow one to analyze the structure of the CME. The bottom row (d–f) contains enhanced-contrast running differences produced by subtraction from each image of

---

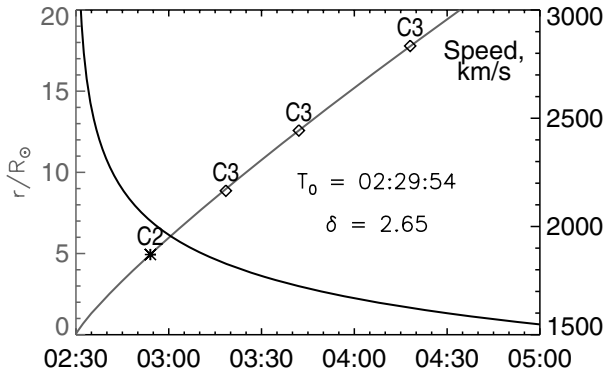[1] ⟨http://cdaw.gsfc.nasa.gov/CME_list⟩.

Fig. 15. Height-time (gray, left axis) and velocity-time (black, right axis) plots of the CME's leading edge fitted as a shock wave. The symbols present measurements in the SOHO LASCO CME Catalog.

the immediately preceding one. Such images reveal the weakest manifestations of the leading edge of a CME, and possibly ahead. However, the appearance of a CME in such images can be different from its real structure, because the subtraction of a preceding image and a heavy enhancement of the contrast produce deceptive effects behind the leading edge (Chertok & Grechnev 2005; Bogachev et al. 2009).

Figures 14a, 14d show a weak suggestion of the streamer at a position angle of $PA \approx 225°$, above the active region 10930 from which the CME originated (this streamer is distinct in images presented in the CME catalog). The images in the top row reveal a complex structure of the transient. The outer radial features could be partly due to deflected coronal rays. Some of them, especially around a PA of 180°, look like loops, which suggests that they were probably constituted by an expanding arcade. Transversal structures are visible inside the presumable arcade. The brightest part of the CME extended approximately from AR 10930 along the streamer, probably being a core flux rope. Keeping in mind that the CME was formed from four sequential eruptions, and most likely contained an expanding pre-eruption arcade, one might find some associated features in the CME, while we have not tried to establish their one-to-one correspondence. Overall, expectations from the eruptions in AR 10930 appear to correspond to the CME structural components and their orientations.

Figures 14d–14e reveal indications of a shock wave propagating ahead of the CME body. The images in figures 14d, 14e resemble an umbrella blowed by strong wind from the inside. The shock conspicuously deflected large streamers in figures 14e, 14f, while the outer trace of its front is outlined by a faint halo edge of the transient. A portion of the flux rope core with a central $PA \approx 225°$ is visible in these two images.

Measurements in the CME catalog refer to the fastest feature of an observed transient. The measurements in the catalog for this CME, carried out at a position angle of $\approx 193°$, are most likely related to the shock. Figure 15 presents the measurements from the catalog (symbols and left axis) along with the gray fit calculated for shock wave propagation. The descending black curve and the right axis present the corresponding velocity-time plot.

The optimizing software found a density falloff exponent of

$\delta = 2.65$, corresponding to the mid-latitude Saito model (Saito 1970), and a shock onset time of about 02:30 (at the position of AR 10930). This result is consistent with an expectation that after some time the upwards-propagating sections of the two shocks following each other (shock 1 excited by eruption EF2 and shock 2 excited by eruption EF3) should merge into a single faster shock with a seemingly later onset time (Grechnev et al. 2011a). This effect is schematically similar to the situation where two pistons located close to each other are substituted by a single piston, which sharply increases its expansion speed twice. After a transition process, a single shock would remain instead of two. This circumstance also hints at a possibility of the earliest shock produced by the eruption of EF1 at about 02:21, which was probably reached by the shock produced by eruption EF2, and merged into a single strong shock 1. This possibility is in accordance with the assumption of Asai et al. (2008) that their blue-shifted feature BS2 observed at 02:23:14 was related to a shock.

A comparison of figures 14b and 14e shows that heavy image processing has exaggerated the weight of the arcade-like component, so that the visible central position angle of the transient looks more like $\approx 190°$. This illusive offset of the CME relative to the position angle of the parent active region was a subject of concern of Sterling et al. (2011), and forced the authors to conclude that the major eruption occurred away from strong magnetic fields. However, non-subtracted images in figures 14a–14c show that the major flux rope of the CME expanded nearly radially above the active region, along the corresponding streamer. The eruptions and flare occurred in the strongest magnetic fields, and the course of the flare appears to be well described by the standard model.

4. Discussion

The preparation of the extreme 2006 December 13 event was indicated by a long-lived microwave neutral line source observed for one week before. The extreme properties of the event were determined by the fact that the eruptions and flare occurred in the strongest magnetic fields above the sunspot umbrae. The umbra of the smaller southern sunspot was entirely covered by the flare ribbon. The other ribbon noticeably intruded into the umbra of the larger northern sunspot. These facts and properties of the flare indicate involvement in the reconnection of large magnetic flux, and agree with the conclusion of Jing et al. (2008) that "*high-energy release regions tend to be concentrated in local strong field regions.*"

Previously, extreme properties of sunspot-associated flares were reported by Grechnev et al. (2008a) and Kundu et al. (2009). According to their conclusions, strong emissions in hard X-rays and gamma-rays are also expected in such events. There is no corresponding information for the 2006 December 13 event. To our knowledge, the only detector of hard electromagnetic emissions in 2006 was RHESSI, but it did not observe the strongest first flare peak due to nighttime (see figure 1f).

An analysis of various aspects of the 2006 December 13 event sheds light on some long-standing issues. One of them is related to a deviation from the Neupert effect.

4.1. The Neupert Effect

From a comparison of 1-min GOES data with a total flux time profile at 15.4 GHz, Struminsky and Zimovets (2008) came to a conclusion drawn concerning a deviation of the emission in this event due to the Neupert effect (Neupert 1968). To investigate into this issue, we used 3-sec GOES data. Their discrete 'staircase' character disfavoring differentiation was overcome by means of a smooth cubic spline approximation with cross-validation for estimating the smoothing parameter. The result presented in figure 1b demonstrates that the derivative of the 0.5–4 Å channel responded to the first (02:25:11) and third (02:32:30) peaks, while the second peak at 02:29:00 was absent. The derivative of the 1–8 Å channel is inconclusive, because a peak indicated by a question mark is most likely an artifact. Indeed, there was a deviation from the Neupert effect, which Struminsky and Zimovets (2008) explained by "*an effective escape of accelerated particles into interplanetary space rather than their precipitation into dense layers of the solar atmosphere*." However, if accelerated electrons escaped, then no corresponding microwave peak occurred, and the Neupert effect worked perfectly in such a case. The strong flux of precipitating electrons is evidenced by the strong hard X-ray burst at that time shown in figure 1f.

A reason for the deviation from the Neupert effect is apparently due to some deficiency of the soft X-ray emission. This emission is produced by evaporated plasmas confined in closed coronal structures. The next eruption most likely opened some of them, and thus releasing confined thermal plasma. An expansion of the escaping plasma should dramatically reduce the emission measure in soft X-rays, and diminish the second peak in the derivative. Thus, a deviation from the Neupert effect in a multi-peak event might be indicative of an additional eruption. Furthermore, the presence of two or more major peaks in the hard X-ray or microwave time profile of a flare might be indicative of more than one eruption. This conjecture is supported by the fact that more than one type II burst are registered in some events.

4.2. Shock Waves

Accordingly, at least, two (or possibly even three) shock waves developed in the 2006 December 13 event. The onset times of shock 1 and shock 2 correspond to the acceleration peaks of two eruptive features, EF2 and EF3, respectively. Both shocks developed about 2 min before the corresponding flare peaks. The initial positions of the shock-wave centers confirm their association with the eruptions. Being excited by the impulsive-piston mechanism, the shock waves detached from the pistons, and quasi-freely propagated for some time, like decelerating blast waves. Manifestations of the two shocks following each other in EUV images and in the dynamic radio spectrum correspond to each other. Local deviations of the wave fronts in regions of increased fast-mode speed from isotropic propagation and progressive displacement of the wave centers toward the coronal hole confirm their MHD wave nature. All of these circumstances strongly support the expectations of Grechnev et al. (2011a) for the development and evolution of shock waves.

Attrill et al. (2010) studied the evolution of coronal dimmings starting from their appearance, and especially the post-CME recovery in two events, one of which was 2006 December 13. The authors considered a possibility for remote dimmings (which they called secondary) to be formed due to the pass of the shock front. This mechanism was assessed to be insufficient to account for long-lived dimmings, because the consequences of a shock wave were considered to be reversible at short time scales, like those of weak disturbances.

However, figure 11 clearly shows that the expansion of the zone of dimming was directly associated with the propagation of the coronal shock wave over the solar surface. The wave front is a moving boundary of a large-scale MHD flow, which accompanies the expansion and eruption of magnetic structures associated with a CME drawing away from the Sun. At the stage when the CME is formed and accelerates, this flow has the character of a lateral expansion of coronal magnetoplasmas, being similar to blowing wind directed outward. The consequences of this flow for a coronal loop depend on its size and orientation. The lower portion of the wave front is tilted toward the solar surface (Uchida 1968; Afanasyev & Uralov 2011), and therefore low loops and filaments should initially be pressed sideward-down, thus producing brightenings just behind the wave front. A very high coronal loop should be initially displaced sideward-up, like a sail. The stretching of such loops should cause plasma outflow from their basis, thus producing dimmings. The recovery of dimmings formed in such a way requires a considerable time, much longer than the timescale of their appearance. Thus, the development of remote dimmings could also be due to passage of the shock front.

EIT and SXI images of this event have provided a unique opportunity to reveal two shocks following each other along the solar surface. On the other hand, the two shock fronts propagating upwards most likely merged into a single stronger shock, whose propagation is consistent with the observed expansion of the CME's leading edge. The shock monotonically decelerated. The deceleration of a shock front along with a nearly constant established speed of a CME behind it suggests that their extrapolated height-time plots should intersect after some time. The actual outcome depends on the CME speed. If the CME is slow, as was the case in the event addressed by Grechnev et al. (2011b), then the shock should eventually decay into a weak disturbance. If the CME is fast which was the case in the 2006 December 13 event, then the blast-wave-like shock should eventually transform into a bow shock ahead of the CME. The latter scenario is confirmed by velocity profiles of shocks ahead of interplanetary CMEs (ICMEs) measured in situ at large distances from the Sun. These velocity profiles are typical of bow shocks continuously pushed by trailing pistons. This was also the case for the interplanetary shock wave developed in the 2006 December 13 event analyzed in detail by Liu et al. (2008), who followed its subsequent propagation up to 2.73 au.

The excitation of shock waves and their evolution turns out to be more complex than traditionally assumed. The presumption of a 'CME-driven shock' directly excited exceptionally in the bow-shock scenario by the outer CME surface at a considerable height well after the flare appears to be a misleading oversimplification. Case studies of very different events with

importance from less than GOES C-class (see Grechnev et al. 2011a) up to the extreme X-class event in the present study confirm the same impulsive-piston shock formation inside a developing CME. Actually, sharp MHD disturbances, which transform into shock waves, appear at the rise phase of a hard X-ray and microwave burst being ready to accelerate particles to high energies, and only dampen and decelerate afterwards. Thus, considerations of relative timing of energetic particles with respect to a flare do not provide any support to their acceleration by shock waves.

The prompt acceleration of protons to high energies simultaneously with electrons during flares has been confirmed in occasional observations of π^0-decay emission, which is generated by $> 300\,\mathrm{MeV}$ protons precipitating into dense layers of the solar atmosphere (Grechnev et al. 2008a; Vilmer et al. 2011; Kurt et al. 2013). On the other hand, the escape of flare-accelerated particles from an active region should be favored by the stretching of closed magnetic configurations during the course of CME lift-off (K.-L. Klein 2011 private communication). If the expanding magnetic flux rope of the CME reconnects with a coronal streamer (e.g., above the parent active region), then the particles trapped in the flux rope gain access to magnetic fields that open into interplanetary space (see also Aschwanden 2012). For this reason, the presence of an apparent delay of particle release near the Sun after the flare seems to favor particle acceleration in the flare, rather than by a shock.

4.3. Comments on Comparison of GLE69 and GLE70

As mentioned, the 70-th ground level enhancement (GLE) of the cosmic-ray intensity produced by the 2006 December 13 event was analyzed in several studies (e.g., Reames 2009; Li et al. 2009; Aschwanden 2012; Nitta et al. 2012). The conclusions about a possible solar source of GLE particles are different. Some of them allow contributions from both flare-related and shock-related acceleration, and some others favor the only certain source. A number of studies endeavors to reach certain conclusions in statistical or comparative analyses.

Such a comparative analysis has been undertaken by Firoz et al. (2011, 2012), who compared the 2006 December 13 event responsible for GLE70 with the 2005 January 20 event responsible for GLE69. The authors' conclusions are nearly opposite for these two events, while our results as well as those of Grechnev et al. (2008a) for the GLE69 event appear to be very similar. In particular, flares in both events occurred in very strong magnetic fields above the umbrae of sunspots, and produced very strong microwave bursts with peak frequencies exceeding 25 GHz. The major circumstances that have led Firoz et al. (2011, 2012) to contrasting these two events are as follows:

1. Hard X-ray and gamma-ray emissions were considerably stronger in the event responsible for GLE69 with respect to the GLE70 event.
   – However, there is no information about these emissions in the strongest peak on 2006 December 13 because of RHESSI nighttime (figure 1f).
2. The relative timing of particle injection and flare emissions disfavor their association.

– Such considerations are inconsistent due to the preceding item and conclusions in subsection 4.2.
3. The GLE69-related CME was considerably slower ($882\,\mathrm{km\,s^{-1}}$) than the GLE70-related one ($1773\,\mathrm{km\,s^{-1}}$).
   – Indeed, the SOHO LASCO CME Catalog presents the speed of $882\,\mathrm{km\,s^{-1}}$ for the 2005 January 20 event, but with a note that it might be underestimated due to strong contamination of LASCO images by energetic particles. The note refers to an estimate of Gopalswamy et al. (2005) of $3242\,\mathrm{km\,s^{-1}}$. Different estimates for the speed of this CME presented by Grechnev et al. (2008a) range from 2000 to $2600\,\mathrm{km\,s^{-1}}$. Thus, the situation was opposite to the assumption of Firoz et al. (2011, 2012): the GLE69-related CME was considerably faster than the GLE70-related one.
4. The type II burst (in a range of 0.1–1 MHz) in the GLE69 event was 'less dynamic' than that in the GLE70 event.
   – Such a comparison should necessarily refer to locations of the emission sources. Grechnev et al. (2011a) have confirmed the idea of Uralova and Uralov (1994) that a type II emission appears in a flare-like process running along the current sheet of a coronal streamer stressed by a shock front. The images of the 2005 January 20 event in the CME Catalog show plasma outflow in both western streamers closest to the eruption site. These streamers probably could not generate the type II burst. Its source region could be in a remote eastern streamer. Before reaching it, the flank of the shock wave should have been considerably decelerated. On the other hand, no obstacles are seen for the appearance of a type II burst from the closest western streamers in the 2006 December 13 event.

There is no convincing reason for contrasting the events responsible for GLE69 and GLE70. The solar events were rather similar in their major properties, which determined their extremeness, while several qualitative and quantitative differences were certainly present.

5. Conclusion

Our multi-spectral analysis of the extreme 2006 December 13 event involving microwave total flux measurements and imaging data has revealed its important properties. The observations along with their quantitative descriptions constitute a consistent picture of the event, which clearly shows the following:

1. The development of this eruptive flare appears to be well-described by the standard model. The flare arcade developed during the course of a few eruptions.
2. The flare episodes were caused by the eruptions being delayed after them. The repetitive eruptions additionally opened the coronal configuration, permitting the escape of evaporated plasmas. This has resulted in a deviation from the Neupert effect.
3. The flare emissions were strongest and hardest when flaring occurred in the strongest magnetic fields above the sunspot umbrae.

4. At least two shock waves were excited by the eruptions as impulsive pistons inside a developing CME and before the related flare peaks. Then, the shock waves quasi-freely propagated like decelerating blast waves.

5. The two shock waves propagating upward most likely merged into a single stronger shock, which constituted the outer halo envelope of the CME, and only decelerated within the LASCO field of view. Transition into the bow-shock regime most likely occurred at a larger distance from the Sun.

On the other hand, the analysis and considerations provide a better understanding of what microwaves show. The strong dependence of the energy release on the magnetic field strength emphasizes emissions from strong-field regions. They are additionally emphasized by the strong dependence on the magnetic field of the microwave emission. As subsection 3.3 has demonstrated, weaker microwave sources should not be neglected, since they show important parts of the flare configuration and its development.

This extreme event confirms conclusions about the nature of coronal shock waves drawn by Grechnev et al. (2011a) based on observations of weaker events. The shock-wave nature of the disturbances observed in this event is confirmed by the close quantitative correspondence of their development to the expected propagation of shock waves, whose excitation coincided in time and space with the strongest accelerations of eruptive flux ropes. Those were near-surface "EUV waves," tracers of the type II bursts, and the leading edge of the CME. These disturbances were super-Alfénic, at least, during some time after their appearance, and only decelerated afterwards.

The scenario revealed for the event disagrees with the delayed CME-driven bow-shock hypothesis: the shock developed much earlier, and could accelerate protons before the flare peak. The delayed particle release time, which is sometimes inferred with respect to the flare, can actually be due to an expansion of the CME magnetic rope, where accelerated particles are trapped. They can be released when the rope reconnects with a streamer. Thus, the late particle release time is not a consistent argument in favor of exceptional shock-acceleration of solar energetic particles.

References

Afanasyev, A. N., & Uralov, A. M. 2011, Sol. Phys., 273, 479

Afanasyev, A. N., Uralov, A. M., & Grechnev, V. V. 2013, Astron. Rep., 57, 594

Afraimovich, E. L., Demyanov, V. V., Gavrilyuk, N. S., Ishin, A. B., & Smolkov, G. Y. 2009b, Cosmic Res., 47, 126

Afraimovich, E. L., Demyanov, V. V., & Smolkov, G. Y. 2009a, Earth, Planets, Space, 61, 637

Antiochos, S. K., DeVore, C. R., & Klimchuk, J. A. 1999, ApJ, 510, 485

Asai, A., Hara, H., Watanabe, T., Imada, S., Sakao, T., Narukage, N., Culhane, J. L., & Doschek, G. A. 2008, ApJ, 685, 622

Asai, A., Masuda, S., Yokoyama, T., Shimojo, M., Isobe, H., Kurokawa, H., & Shibata, K. 2002, ApJ, 578, L91

Asai, A., Yokoyama, T., Shimojo, M., Masuda, S., Kurokawa, H., & Shibata, K. 2004, ApJ, 611, 557

Aschwanden, M. J. 2012, Space Sci. Rev., 171, 3

Attrill, G. D. R., Harra, L. K., van Driel-Gesztelyi, L., & Wills-Davey, M. J. 2010, Sol. Phys., 264, 119

Bogachev, S. A., Grechnev, V. V., Kuzin, S. V., Slemzin, V. A., Bugaenko, O. I., & Chertok, I. M. 2009, Sol. Syst. Res., 43, 143

Carmichael, H. 1964, in Proc. AAS-NASA Symp., The Physics of Solar Flares, ed. W. N. Hess, NASA-SP 50 (Washington D.C.: NASA), 451

Chen, J. 1989, ApJ, 338, 453

Chertok, I. M., & Grechnev, V. V. 2005, Sol. Phys., 229, 95

Cliver, E. W., Kahler, S. W., Shea, M. A., & Smart, D. F. 1982, ApJ, 260, 362

Dulk, G. A., & Marsh, K. A. 1982, ApJ, 259, 350

Firoz, K. A., Gan, W. Q., Moon, Y.-J., & Li, C. 2012, ApJ, 758, 119

Firoz, K. A., Moon, Y.-J., Park, S.-H., Kudela, K., Islam, J. N., & Dorman, L. I. 2011, ApJ, 743, 190

Golub, L., et al. 2007, Sol. Phys., 243, 63

Gopalswamy, N., Xie, H., Yashiro, S., & Usoskin, I. 2005, in Proc. 29th Int. Cosmic Ray Conf. Vol. 1, ed. B. Sripathi et al. (Mumbai: Tata Institute of Fundamental Research), 169

Grechnev V. V., et al. 2008a, Sol. Phys., 252, 149

Grechnev, V., Afanasyev, A., Uralov, A., Kuzmenko, I. V., Afanasyev, A. N., Meshalkina, N. S., Kalashnikov, S. S., & Kubo, Y. 2011b, Sol. Phys., 273, 461

Grechnev, V. V., Uralov, A. M., Chertok, I. M., Chertok, I. M., Eselevich, M. V., Eselevich, V. G., Rudenko, G. V., & Kudo, Y. 2011a, Sol. Phys., 273, 433

Grechnev, V. V., Uralov, A. M., Slemzin, V. A., Chertok, I. M., Filippov, B. P., Rudenko, G. V., & Temmer, M. 2014, Sol. Phys., 289, 289

Grechnev, V. V., Uralov, A. M., Slemzin, V. A., Chertok, I. M., Kuzmenko, I. V., & Shibasaki, K. 2008b, Sol. Phys., 253, 263

Hirayama, T. 1974, Sol. Phys., 34, 323

Hudson, H. S., & Webb, D. F. 1997, in Coronal Mass Ejection, ed. N. Crooker et al. (Washington D. C.: AGU), 27

Imada, S., Hara, H., Watanabe, T., Kamio, S., Asai, A., Matsuzaki, K., Harra, L. K., & Mariska, J. T. 2007, PASJ, 59, S793

Imada, S., Hara, H., Watanabe, T., Murakami, I., Harra, L. K., Shimizu, T., & Zweibel, E. G. 2011, ApJ, 743, 57

Jin, M., Ding, M. D., Chen, P. F., Fang, C., & Imada, S. 2009, ApJ, 702, 27

Jing, J., Chae, J., & Wang, H. 2008, ApJ, 672, L73

Kallenrode, M.-B. 2003, J. Phys. G, 29, 965

Kintner, P. M., O'Hanlon, B., Gary, D. E., & Kintner, P. M. S. 2009, Radio Science, 44, RS0A08

Klein, K.-L., & Trottet, G. 2001, Space Sci. Rev., 95, 215

Kopp, R. A., & Pneuman, G. W. 1976, Sol. Phys., 50, 85

Kosugi, T., et al. 2007, Sol. Phys., 243, 3

Kundu, M. R., Grechnev, V. V., White, S. M., Schmahl, E. J., Meshalkina, N. S., Kashapova, L. K. 2009, Sol. Phys., 260, 135

Kurt, V., Yushkov, B., Belov, A., Chertok, I., Grechnev, V. 2013, J. Phys. Conf. Ser., 409, 012151

Kusano, K., Bamba, Y., Yamamoto, T. T., Iida, Y., Toriumi, S., & Asai, A. 2012, ApJ, 760, 31

Li, C., Dai, Y., Vial, J.-C., Owen, C. J., Matthews, S. A., Tang, Y. H., Fang, C., & Fazakerley, A. N. 2009, A&A, 503, 1013

Liu, Y., et al. 2008, ApJ, 689, 563

Mandrini, C. H., Pohjolainen, S., Dasso, S., Green, L. M., Démoulin, P., van Driel-Gesztelyi, L., Copperwheat, C., & Foley, C. 2005, A&A, 434, 725

Mann, G., Klassen, A., Aurass, H., & Classen, H.-T. 2003, A&A, 400, 329

Maričić, D., Vršnak, B., Stanger, A. L., Veronig, A. M., Temmer, M., & Roša, D. 2007, Sol. Phys., 241, 99

Moore, R. L., Sterling, A. C., Hudson, H. S., & Lemen, J. R. 2001, ApJ, 552, 833

Nakajima, H., et al. 1985, PASJ, 37, 163

Nakajima, H., et al. 1994, Proc. IEEE, 82, 705

Neupert, W. M. 1968, ApJ, 153, L59

Ning, Z. 2008, Sol. Phys., 247, 53

Nita, G. M., Fleishman, G. D., Jing, J., Lesovoi, S. V., Bogod, V. M., Yasnov, L. V., Wang, H., & Gary, D. E. 2011, ApJ, 737, 82

Nitta, N. V., Liu, Y., DeRosa, M. L., & Nightingale, R. W. 2012, Space Sci. Rev., 171, 61

Reames, D. V. 1999, Space Sci. Rev., 90, 413

Reames, D. V. 2009, ApJ, 693, 812

Saito, K. 1970, Ann. Tokyo Astron. Obs., 12, 53

Smolkov, G. Y., Uralov, A. M., & Bakunina, I. A. 2009, Geomagn. Aeron., 49, 1101

Sterling, A. C., & Hudson, H. S. 1997, ApJ, 491, L55

Sterling, A. C., Moore, R. L., & Harra, L. K. 2011, ApJ, 743, 63

Struminsky, A. B., & Zimovets, I. V. 2008, Astron. Lett., 34, 704

Sturrock, P. A. 1966, Nature, 211, 695

Suematsu, Y., et al. 2008, Sol. Phys., 249, 197

Temmer, M., Veronig, A. M., Kontar, E. P., Krucker, S., & Vršnak, B. 2010, ApJ, 712, 1410

Temmer, M., Veronig, A. M., Vršnak, B., Rybák, J., Gömöry, P., Stoiser, S., & Maričić, D. 2008, ApJ, 673, L95

Torii, C., Tsukiji, Y., Kobayashi, S., Yoshimi, N., Tanaka, H., & Enome, S. 1979, Proc. Res. Inst. Atmos. Nagoya Univ., 26, 129

Tsuneta S., et al. 2008, Sol. Phys., 249, 167

Uchida, Y. 1968, Sol. Phys., 4, 30

Uralov, A. M., Grechnev, V. V., Rudenko, G. V., Rudenko, I. G., & Nakajima, H. 2008, Sol. Phys., 249, 315

Uralov, A. M., Lesovoi, S. V., Zandanov, V. G., & Grechnev, V. V. 2002, Sol. Phys., 208, 69

Uralov, A. M., Rudenko, G. V., & Rudenko, I. G. 2006, PASJ, 58, 21

Uralova, S. V., & Uralov, A. M. 1994, Sol. Phys., 152, 457

Vilmer, N., MacKinnon, A. L., & Hurford, G. J. 2011, Space Sci. Rev., 159, 167

Webb, D. F., Lepping, R. P., Burlaga, L. F., DeForest, C. E., Larson, D. E., Martin, S. F., Plunkett, S. P., & Rust, D. M. 2000, J. Geophys. Res., 105, 27251

White, S. M., Krucker, S., Shibasaki, K., Yokoyama, T., Shimojo, M., & Kundu, M. R. 2003, ApJ, 595, L111

Yashiro, S., Gopalswamy, N., Michałek, G., St. Cyr, O. C., Plunkett, S. P., Rich, N. B., & Howard, R. A. 2004, J. Geophys. Res., 109, A07105

Zhang, J., Dere, K. P., Howard, R. A., Kundu, M. R., & White, S. M. 2001, ApJ, 559, 452